THE LABOCA SURVEY OF THE EXTENDED CHANDRA DEEP FIELD SOUTH: TWO MODES OF STAR FORMATION IN ACTIVE GALACTIC NUCLEUS HOSTS?

D. Lutz[1], V. Mainieri[2], D. Rafferty[3], L. Shao[1], G. Hasinger[4], A. Weiß[5], F. Walter[6], I. Smail[7], D. M. Alexander[8], W. N. Brandt[3], S. Chapman[9], K. Coppin[7], N. M. Förster Schreiber[1], E. Gawiser[10], R. Genzel[1], T. R. Greve[6], R. J. Ivison[11,12], A. M. Koekemoer[13], P. Kurczynski[10], K. M. Menten[5], R. Nordon[1], P. Popesso[1], E. Schinnerer[6], J. D. Silverman[14], J. Wardlow[8], AND Y. Q. Xue[3]

[1] Max-Planck-Institut für extraterrestrische Physik, Postfach 1312, 85741 Garching, Germany; lutz@mpe.mpg.de
[2] European Southern Observatory, Karl-Schwarzschild-Straße 2, 85748 Garching, Germany
[3] Department of Astronomy and Astrophysics, 525 Davey Lab, Pennsylvania State University, University Park, PA 16802, USA
[4] Max-Planck-Institut für Plasmaphysik, Boltzmannstraße 2, 85748 Garching, Germany
[5] Max-Planck-Institut für Radioastronomie, Auf dem Hügel 69, 53121 Bonn, Germany
[6] Max-Planck-Institut für Astronomie, Königstuhl 17, 69117 Heidelberg, Germany
[7] Institute for Computational Cosmology, Durham University, South Road, Durham, DH1 3LE, UK
[8] Department of Physics, Durham University, South Road, Durham, DH1 3LE, UK
[9] Institute of Astronomy, Madingley Road, Cambridge, CB3 0HA, UK
[10] Physics & Astronomy Department, Rutgers University, Piscataway, NJ 08854, USA
[11] SUPA, Institute for Astronomy, University of Edinburgh, Royal Observatory, Blackford Hill, Edinburgh, EH9 3HJ, UK
[12] UK Astronomy Technology Centre, Royal Observatory, Blackford Hill, Edinburgh, EH9 3HJ, UK
[13] Space Telescope Science Institute, 3700 San Martin Drive, Baltimore, MD 21218, USA
[14] Institute for the Physics and Mathematics of the Universe (IPMU), University of Tokyo, Kashiwanoha 5-1-5, Kashiwa, Chiba 277-8568, Japan
Received 2009 August 29; accepted 2010 February 16; published 2010 March 12

ABSTRACT

We study the co-existence of star formation and active galactic nucleus (AGN) activity in *Chandra* X-ray-selected AGN by analyzing stacked $870\,\mu$m submillimeter emission from a deep and wide map of the Extended Chandra Deep Field South (ECDFS), obtained with the LABOCA instrument at the APEX telescope. The total X-ray sample of 895 sources with median redshift $z \sim 1$ drawn from the combined (E)CDFS X-ray catalogs is detected at $>11\sigma$ significance at a mean submillimeter flux of 0.49 ± 0.04 mJy, corresponding to a typical star formation rate (SFR) around $30\,M_\odot\,\mathrm{yr}^{-1}$ for a $T = 35$ K, $\beta = 1.5$ graybody far-infrared spectral energy distribution. The good signal-to-noise ratio permits stacking analyses for major subgroups, splitting the sample by redshift, intrinsic luminosity, and AGN obscuration properties. We observe a trend of SFR increasing with redshift. An increase of SFR with AGN luminosity is indicated at the highest $L_{2-10\,\mathrm{keV}} \gtrsim 10^{44}$ erg s^{-1} luminosities only. Increasing trends with X-ray obscuration as expected in some AGN evolutionary scenarios are not observed for the bulk of the X-ray AGN sample but may be present for the highest intrinsic luminosity objects with $L_{2-10\,\mathrm{keV}} \gtrsim 10^{44}$ erg s^{-1}. This behavior suggests a transition between two modes in the co-existence of AGN activity and star formation. For the bulk of the sample, the X-ray luminosity and obscuration of the AGN are not intimately linked to the global SFR of their hosts. The hosts are likely massive and forming stars secularly, at rates similar to the pervasive star formation seen in massive galaxies without an AGN at similar redshifts. In these systems, star formation is not linked to a specific state of the AGN and the period of moderately luminous AGN activity may not highlight a major evolutionary transition of the galaxy. The change indicated toward more intense star formation, and a more pronounced increase in SFRs between unobscured and obscured AGN reported in the literature at highest $(L_{2-10\,\mathrm{keV}} \gtrsim 10^{44}$ erg s$^{-1})$ luminosities suggests that these luminous AGNs follow an evolutionary path on which obscured AGN activity and intense star formation are linked, possibly via merging. Comparison to local hard X-ray-selected AGN supports this interpretation. SFRs in the hosts of moderate luminosity AGN at $z \sim 1$ are an order of magnitude higher than at $z \sim 0$, following the increase in the non-AGN massive galaxy population. At high AGN luminosities, hosts on the evolutionary link/merger path emerge from this secular level of star formation.

Key words: galaxies: active – galaxies: starburst – infrared: galaxies

Online-only material: color figures

1. INTRODUCTION

Observing the co-evolution of active galactic nuclei (AGNs) and their hosts is key to understanding the similar cosmic evolution of the space density of luminous AGN and of the star formation rate (SFR) density. This co-evolution also has to lead to today's fossil relations between remnant supermassive black hole mass and the properties of the host spheroid. Directly measuring the SFR of a high-redshift galaxy is however particularly difficult for AGN hosts, since the AGN proper will disturb and overwhelm the rest-frame UV and optical spectral and photo-

metric star formation tracers already at modest luminosities, unless the AGN is obscured. Furthermore, star formation in the host may be noticeably obscured in particular at high SFRs approaching that of high-redshift ultraluminous infrared and submillimeter galaxies. Infrared observations can thus play an important role for these studies. One approach that has been successfully applied to high-redshift AGNs is to use the mid-infrared polycyclic aromatic hydrocarbon (PAH) emission features which can be separated from the strong AGN mid-IR continuum emission by means of low resolution spectroscopy (e.g., Houck et al. 2005; Lutz et al. 2005). However, even with the

superb spectroscopic sensitivity of the *Spitzer Space Telescope*, this approach is limited for high redshifts to modest sample sizes. Alternatively, observations of the rest-frame far-infrared/submillimeter continuum have been used since the advent of the first sensitive submillimeter photometers to measure star formation via the far-infrared/submillimeter continuum from the associated cool ($T \sim 35$ K) dust. This rests on the submillimeter continuum being due to star formation in the host galaxy, with star formation dominating over the AGN heated dust emission at these wavelengths for all but the highest ratios of AGN luminosity to star formation in the host. Such a star formation dominance in the submillimeter is possible because of the steep decline of AGN dust emission toward far-infrared and submillimeter wavelengths (e.g., Pier & Krolik 1992, and later torus models), while the spectral energy distributions (SEDs) of star-forming galaxies have a pronounced far-infrared (FIR) peak. The assumption of star formation dominating the submillimeter emission is supported by several types of observations. For NGC 1068, the AGN in the local universe for which current spatial resolution is sufficient to separate the AGN from the host in the far-infrared/submillimeter range, this assumption is directly supported by observations (Pier & Krolik 1993; Papadopoulos & Seaquist 1999; Le Floc'h et al. 2001). Note that NGC 1068 falls well into the range of AGN luminosities (intrinsic $L_{2-10 \text{keV}} \sim 10^{43.5}$ erg s^{-1}; Colbert et al. 2002) and far-infrared luminosities ($L_{\text{IR}} \sim 10^{11.3} L_\odot$) of the AGNs found in deep X-ray surveys, such as the (E)CDFS AGNs that are discussed below. Recent *Spitzer* spectroscopic studies using the PAH emission features in comparison to the far-infrared/submillimeter emission lend further support to this assumption, indicating that, at $L_{\text{AGN}}/L_{\text{FIR}} \sim 10$, the far-infrared emission of local QSOs as well as of millimeter-bright high-redshift QSOs is dominated by star formation in the host (Schweitzer et al. 2006; Netzer et al. 2007; Lutz et al. 2008), plausibly fed by large reservoirs of molecular gas (e.g., Evans et al. 2001; Solomon & VandenBout 2005). Here, we study a sample that is at or below this ratio of AGN and star-forming luminosities (Section 3.2). Our sample does not reach the extreme values as some of the most luminous but millimeter-faint high-z QSOs, for which the assignment of far-infrared emission to star formation is more uncertain (see discussion in Lutz et al. 2008). Our sample is X-ray-selected and thus not biased toward extremely obscured infrared objects as, e.g., some local ULIRGs or high-redshift dust-obscured galaxies (e.g., Houck et al. 2005), for which the AGN contribution to the far-infrared emission may be significant.

Measuring the submillimeter emission and on its basis the SFR of AGN hosts thus plays an important role in constraining the evolution of AGNs. Such studies directly benefit from the improving depth and areal coverage of current submillimeter surveys. Both, the study of local AGNs and of the AGN/galaxy (co)evolution have led to the suggestion of models in which intense star formation events and powerful AGN activity are physically linked and sequentially occur in a single object (e.g., Sanders et al. 1988; Fabian 1999; Granato et al. 2004; Hopkins et al. 2006), in a process closely linked to the hierarchical merging of galaxies in the universe. In a nutshell, galaxy interaction followed by merging with associated gas inflow may trigger a powerful burst of star formation and subsequently feed the central black hole(s) of the merger, to produce a luminous AGN. The AGN may then quench the star formation event and shed the obscuring dust, and finally emerge as an optically visible QSO. In this evolutionary picture, an obscured AGN would sample the earlier phases of the AGN activity and would be associated with more powerful star formation in the AGN host, and thus stronger submillimeter emission. As already implied by the typically non-merger morphology of local moderate-luminosity AGNs (Seyferts), such an evolutionary picture may not always apply and its applicability needs to be studied as a function of AGN luminosity and redshift.

A different behavior would be expected in the context of the successful unified picture of AGNs proper, in which the differences between obscured and unobscured types of AGNs are the consequences of different viewing directions on intrinsically identically structured systems. In fact, for the AGN and its immediate dusty surroundings, for example, in the form of a "torus," emission would be expected to be equally strong or stronger in the face-on/unobscured direction compared to the edge-on direction, even at long far-infrared or submillimeter wavelengths (e.g., Pier & Krolik 1992; Nenkova et al. 2008). However, because of the intrinsically weaker AGN/torus emission at far-infrared and submillimeter wavelengths, such differences will be easily washed out by even a modest amount of star formation in the host galaxy. This would lead to the expectation of little dependency of submillimeter emission to obscuration in the unified AGN picture. This "unified" view is by no means contradictory to the evolutionary picture. Considering both these perspectives only stresses that differences in submillimeter emission found between different AGN types will to a large extent reflect evolutionary coupling of periods of AGN activity and host star formation, rather than AGN physics and orientation alone. If evolutionary signatures are found in the sbmillimeter, the underlying mechanisms like merging have to be clarified from additional information like morphology or dynamics. Combining evolutionary and unified perspectives also emphasizes the need to separately test for possible evolutionary effects in populations of high-redshift AGNs of different luminosities, that may follow different paths of AGN and host evolution.

First looks at the submillimeter emission of X-ray-selected AGNs have compared deep X-ray surveys to the first generation of (sub)millimeter surveys (e.g., Fabian et al. 2000; Severgnini et al. 2000; Hornschemeier et al. 2000; Barger et al. 2001; Almaini et al. 2003; Waskett et al. 2003). In general, no straightforward correspondence between typical sources from these X-ray surveys and bright submillimeter sources detected with SCUBA (Holland et al. 1999) was established, and the average flux from submillimeter stacking experiments of X-ray AGNs was found to be low, e.g., $S_{850 \mu m} = 1.21 \pm 0.27$ mJy for the Chandra Deep Field North (CDFN; Barger et al. 2001) and $S_{850 \mu m} = 0.48 \pm 0.27$ mJy from the Canada-UK Deep SCUBA Survey (CUDSS) (Waskett et al. 2003), with insufficient signal-to-noise ratio (S/N) of the stacks for an in-depth analysis as a function of AGN properties. Pointed submillimeter follow-up of selected, e.g., hard/luminous sources from the deep X-ray surveys resulted in a few detections (e.g., Mainieri et al. 2005a; Rigopoulou et al. 2009) but also some upper limits. Conversely, SCUBA sources were often found to be associated with X-ray faint AGNs in the very deepest X-ray surveys (Alexander et al. 2005a, 2005b). These faint AGNs do not dominate the energetics of the SCUBA sources and were undetectable in earlier analyses that were not based on the ultradeep 2 Ms *Chandra* data. Their black hole masses appear modest compared to similarly massive galaxies and to more powerful AGNs (Borys et al. 2005; Alexander et al. 2008).

The study that has been perhaps most successful so far in establishing bright submillimeter emission for an X-ray-selected

AGN population and finding trends with AGN properties used a different approach. Selecting luminous X-ray absorbed but optically bright AGNs not from deep field *Chandra* or *XMM-Newton* X-ray survey data but from identification of X-ray brighter sources from the *ROSAT* survey, Page et al. (2001) were able to detect four of eight X-ray absorbed QSOs at $S_{850\,\mu m} > 5$ mJy. Later comparisons with matched X-ray unabsorbed samples (Page et al. 2004; Stevens et al. 2005) provided evidence for a lower submillimeter detection rate of the X-ray unabsorbed objects. This difference in submillimeter brightness between obscured and unobscured objects supports the evolutionary view, but questions remain in particular when comparing the large submillimeter fluxes for some of the Page et al. (2001) objects with the more modest success of submillimeter follow-up observations of luminous hard sources from deep fields. If submillimeter emission follows the emission at other wavelengths, this might simply reflect the brighter observed fluxes and larger AGN luminosities of the Page et al. (2001) sources. However, it should be noted that these are selected as moderately X-ray obscured ($N_H \sim 10^{22}$ cm^{-2}) but optically unobscured (optical broad emission line = Type 1) AGNs, unlike many of the heavily obscured AGNs from deep X-ray fields, which show Type 2 optical spectra lacking broad lines. Like the broad lines, their bright optical magnitudes (Page et al. 2001b) argue against a significant obscuration of the AGNs in the rest-frame optical/UV. Extending such studies to include a more typical obscured AGN is clearly important and a main motivation of this paper.

We here present a study of the submillimeter properties of X-ray-selected AGNs in the (E)CDFS. Making use of a new submillimeter map provided by LABOCA at the APEX facility (Weiß et al. 2009) as well as current X-ray data with substantially improved identification status and characterization of the AGNs, we can study the submillimeter properties and hence host SFRs as a function of AGN properties. Throughout the paper, we adopt an $\Omega_m = 0.3$, $\Omega_\Lambda = 0.7$, and $H_0 = 70$ km s^{-1} Mpc^{-1} cosmology. When distinguishing between moderate luminosity (Seyfert) and high luminosity (QSO) AGNs we refer to an intrinsic luminosity limit of $L_{2-10\,keV} = 10^{44}$ erg s^{-1} unless stated otherwise.

2. RESULTS FROM SUBMILLIMETER MAPPING OF THE EXTENDED CHANDRA DEEP FIELD SOUTH

The excellent X-ray and multiwavelength coverage of the 0.1 deg^2 CDFS and the surrounding 0.3 deg^2 Extended Chandra Deep Field South (ECDFS), in combination with the powerful mapping capabilities of the LABOCA submillimeter camera (Siringo et al. 2009) at the APEX telescope (Güsten et al. 2006), enables us to take a fresh look at the issues discussed in Section 1, making use of the improved observational resources. We use the LABOCA 870 μm map obtained by the LABOCA ECDFS Submm Survey (LESS) consortium as described by Weiß et al. (2009). We use the beam-convolved v2.2 final map which includes a total of about 350 hr of observing time over an area of about $40' \times 40'$ with an rms noise level of about 1.2 mJy beam^{-1} in the inner $30' \times 30'$. This map and the catalog of 126 sources detected at $>3.7\sigma$ is presented in Weiß et al. (2009). We also make use of the residual map obtained by subtracting these 126 sources, using fluxes that consider in a statistical sense the boosting by instrument and confusion noise (Weiß et al. 2009; Coppin et al. 2005).

2.1. Samples of X-ray AGNs

To maximize the statistics and to allow us to draw meaningful conclusions for physically selected subgroups of X-ray-selected AGNs, we use X-ray-based AGN samples from *Chandra* observations for both the ECDFS and the deeper but smaller CDFS, for a total of 895 X-ray sources. For the CDFS, we mainly use X-ray spectral properties of Tozzi et al. (2006) which are related to and based on the original CDFS observations of Giacconi et al. (2002). Recently, the deeper 2 Ms *Chandra* data and catalog for the CDFS have become available (Luo et al. 2008) but physical modeling comparable to the level of Tozzi et al. (2006) is not yet completed (F. E. Bauer et al. 2010, in preparation). We therefore use the updated 2 Ms observational data (observed fluxes, hardness ratios, etc.), from Luo et al. (2008) where available but stick to the Tozzi et al. (2006) results for physical properties derived from X-ray spectral fitting (intrinsic luminosities, X-ray obscuring column density N_H, etc.). We have also added 94 CDFS sources that are new from Luo et al. (2008). Lacking X-ray spectral fitting, these were used only for the combined stack and when analyzing properties as a function of redshift, no modeled properties are available for those. To reduce contamination by non-AGN sources we exclude here objects that are likely nearby normal/star-forming galaxies. Discrimination between such objects and AGNs is approximately possible by comparing their X-ray to their optical properties; specifically we have adopted a cutoff $\log(f_X/f_R) \geqslant -1$ (e.g., Bauer et al. 2004), for the ratio of the X-ray flux to the optical R-band flux. Here we use as X-ray flux the observed full band flux if available, otherwise the larger of hard and soft band flux. For similar reasons, we exclude 14 sources from Tozzi et al. (2006) with intrinsic rest frame $L_{0.5-10\,keV} < 10^{41}$ erg s^{-1}. Sources with such low X-ray luminosities will mostly not be AGNs (e.g., Bauer et al. 2004). We have furthermore excluded 20 sources from Tozzi et al. (2006) that are not re-detected in the deeper 2 Ms data of Luo et al. (2008). In particular, this cut includes the Giacconi et al. (2002) XID 618. While this source, indicated in only one of the two source extraction methods used by Giacconi et al. (2002), is coincident with an interesting $z = 4.76$ submillimeter galaxy (SMG; Coppin et al. 2009), its nature as an X-ray source is not confirmed by the deeper X-ray data of Luo et al. (2008). Including it in our analysis as a luminous obscured X-ray source as inferred by Tozzi et al. (2006) would increase the differences between luminous unobscured and obscured AGNs that we discuss in Section 2.2. The overall CDFS list has 396 X-ray sources out of which 302 have X-ray spectral fitting from Tozzi et al. (2006).

For ECDFS sources outside of the CDFS, we use the X-ray catalog of Lehmer et al. (2005), supplemented with currently available identification and redshift information (J. D. Silverman et al. 2010, in preparation), but not yet including results of Treister et al. (2009). Again, we have imposed a $\log(f_X/f_R) \geqslant -1$ cutoff to reduce contamination by non-AGNs. We avoid double counting objects in the Lehmer et al. (2005) ECDFS catalog that are also CDFS sources. Objects in the Giacconi et al. (2002) CDFS main catalog are identified by a flag in Lehmer et al. (2005). For these we use the CDFS data and spectral fitting only. The Luo et al. (2008) data detect more sources at the edge of the CDFS that are in the Lehmer et al. (2005) catalog but not flagged as also detected in the CDFS. We avoid double counting those by eliminating them via a 5″ radius match and using the ECDFS X-ray data.

For the CDFS sources of Tozzi et al. (2006) we adopt the positions provided in that paper. For the additional sources

from Luo et al. (2008) we use their optical positions where given and X-ray positions otherwise. In the ECDFS, we use optical positions from identifications by V. Mainieri et al. (2010, in preparation) when available and X-ray positions elsewhere. Note that the 27″ FWHM beam of the LABOCA map, obtained after convolution of the raw map with its own beam size of 19″.2 (Weiß et al. 2009), is large compared to the *Chandra* X-ray positional uncertainties even for the least favorable case of modest S/N faint sources at large off-axis angles, reducing the need for optical identifications for the stacking process. Typically, *Chandra* X-ray positions are accurate to well below an arcsec (e.g., Figure 5 of Luo et al. 2008).

We adopt as redshifts for all the CDFS sources of Tozzi et al. (2006) the values given in that paper. About half of these are spectroscopic redshifts from Szokoly et al. (2004) and other references, while the rest are photometric redshifts which benefit from the excellent multiwavelength coverage of the CDFS. For the ECDFS area and the identifications of Mainieri et al., we have used in order of preference (1) secure (e.g., two or more emission lines or clear spectral features, Ca H&K) spectroscopic redshifts from J. D. Silverman et al. (2010, in preparation), (2) other spectroscopic redshifts from the compilation of D. Rafferty et al. (2010, in preparation), (3) photometric redshifts derived by D. Rafferty et al. (2010, in preparation) from a comprehensive compilation of multi-band UV to *Spitzer*-IRAC photometry using the ZEBRA photo-z code, and finally in the remaining 28 cases (4) photometric redshifts from the COMBO-17 survey which provides accurate photometric redshifts using photometry in 17 passbands from 350 to 930 nm. Here we have used the latest version of the COMBO-17 CDFS catalogue, following a calibration update (Wolf et al. 2008). We use this data set with two limitations. We consider only COMBO-17 sources with $R < 24$ (Vega): at these magnitudes the errors on the photometric redshift estimates are expected to be less than $|z_{phot} - z_{spec}|/(1 + z_{spec}) \approx 0.06$. The COMBO-17 data for galaxies fainter than $R = 24$ (Vega) are too shallow for accurate photo-z determination of AGNs. Further, we limit the use of COMBO-17 photometric redshifts to $z < 1.2$ because at higher redshifts the COMBO-17 estimates become increasingly inaccurate due to the lack of NIR coverage (see Section 4.6 of Wolf et al. 2004). We have waived this last constraint for objects best fitted with QSO templates (MC$_{class}$ = "QSO" in Wolf et al. 2004) for which the photometric redshifts are accurate at least to $z \approx 4$ (see Figure 18 of Wolf et al. 2004). In total, we thus have redshifts for about three quarters of the X-ray targets outside the CDFS. For the new Luo et al. (2008) sources we use redshifts from D. Rafferty et al. (2010, in preparation) where available.

The combined CDFS+ECDFS X-ray-based catalog has 895 sources with a median X-ray flux of 3×10^{-16} erg cm^{-2} s^{-1} in the observed soft and 10^{-15} erg cm^{-2} s^{-1} in the hard band. 748 sources have spectroscopic or reliable photometric redshifts in the range up to $z \sim 5$ (median $z = 1.17$), the median observed X-ray luminosity of those sources is 10^{43} erg s^{-1}. In the following we call this the "combined" sample, while with the "CDFS" sample we designate the 302 sources from Tozzi et al. (2006) with X-ray spectral fits, remaining after the cuts described above (median $z = 1.04$).

2.2. Stacking Procedure

We derive average submillimeter fluxes for a given source population by extracting both the map flux (in Jy beam^{-1}) and the map rms noise, using bilinear interpolation to the source position in the beam-convolved LABOCA flux map and noise

map. We then use the inverse variance weighted average of the fluxes measured over the stack.

Stacking procedures for data from large-beam deep submillimeter maps that are approaching the confusion limit at these wavelengths have to consider two effects. First, blank background and thus the "zero point" of a sky image is hard to identify. At the rms noise of ∼1.2 mJy of our data, integral number counts approach 10^4 deg^{-2} (e.g., Coppin et al. 2006), which is only a modest factor away from the LABOCA beam density (2×10^4 deg^{-2} for an area of π HWHM^2 of the convolved beam); see also the discussion in Weiß et al. (2009) on the contribution of confusion noise in the LABOCA map. This means there is effectively no clean background sky. Second, for the large submillimeter beam an elevated signal at the position of a stacked source may originate from the wings of the beam of a nearby unrelated bright submillimeter source. Chopped beam patterns would cause additional complications but do not apply to the scanned LABOCA data that were obtained in total power mode.

We have addressed this situation with simple Monte Carlo simulations, randomly placing ∼10^6 Gaussian beams over a 1000 × 1000 pixel blank image and assuming a beam width (in pixels) equal to the LABOCA beam width. Input fluxes were distributed according to a simplified integral number count distribution with a power-law slope −2 (approximating measurements of, e.g., Coppin et al. 2006; Weiß et al. 2009) and extending 3 orders of magnitude down from the brightest source in the map, deep into confusion. If the simulated image is offset to a mean value 0 and stacking experiments are done using the positions of subsets of the input list, mean fluxes from stacks agree with the mean of the input fluxes within an error estimated from the standard deviation of the image, divided by the square root of the stacked sample size. The noise level of current submillimeter maps and the fact that they do not reach below the knee of the integral counts implies a dynamic range between noise and brightest source of typically about an order of magnitude only. This reduces the effects of individual bright outliers on such error estimates. With a proper image zero point, the effects of the difficulty to define the background and of confusion thus cancel, and stacked fluxes can be used directly. In the LABOCA data, instrument noise is still (just) dominant over confusion noise (Weiß et al. 2009), its presence is again consistent with this stacking procedure. Figure 1 shows the pixel flux histograms for the part of the LABOCA flux map that is within a factor 1.5 from the minimum rms of 1.07 mJy beam^{-1} and for the residual map after subtraction of detected sources (Weiß et al. 2009). In stacking experiments we subtracted the respective means (0.154 mJy beam^{-1} and 0.072 mJy beam^{-1} for this part of the flux and residual map, respectively). This also ensures that zero average flux is returned from stacking random positions in the map. In deriving the stacked fluxes, we also calculate an inverse variance weighted stacked submap which, for stacks with significant detections, can be used to verify that the stacked beam is centered and reproduces the original beam of the map. Spatial clustering of the stacked population can in principle significantly affect source counts and stacking results. The effect on the stacks can be very important for instruments at similar wavelengths with much larger beams than that of APEX, like Planck-HFI (e.g., Negrello et al. 2005). It is negligible for the LABOCA beam at this wavelength (Bavouzet 2009), and hence not considered in our stacking.

We base our discussion on stacking the flux map but also provide stacking results for the residual map for comparison. In
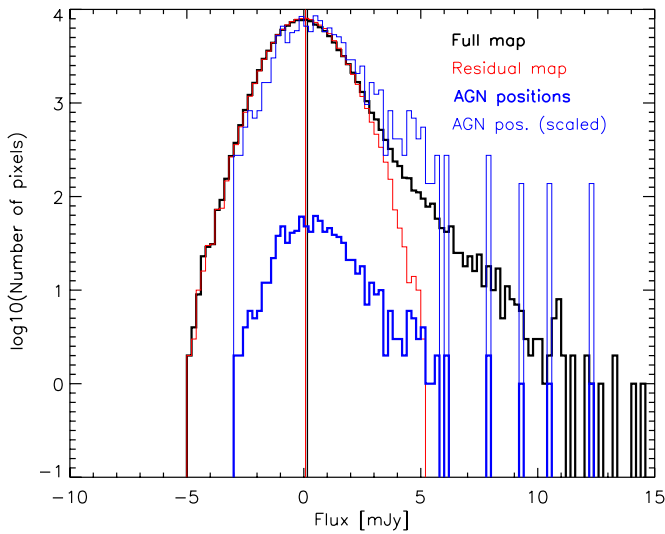
Figure 1. Pixel flux histograms for the roughly 80% of the LABOCA 870 μm map of the ECDFS with rms less than or equal to 1.5 times the minimum noise of 1.07 mJy. The black thick histogram represents the full map, and the red thin histogram the residual map after subtraction of detected sources (Weiß et al. 2009). Vertical lines indicate the mean flux of this region in the respective map. The blue thick histogram shows the flux distribution at the positions of the combined sample of 895 CDFS and ECDFS AGNs. For easy comparison of this AGN histogram to the full map, the blue thin histogram shows it scaled to the number of map pixels.

(A color version of this figure is available in the online journal.)

Figure 2. Stamps showing the co-added LABOCA submillimeter signal for all 895 CDFS and ECDFS X-ray sources in our combined list. Left: obtained using the total LABOCA flux map. The 27″ FWHM beam size of the LABOCA map is shown for comparison in the bottom left. Right: obtained using the residual map after subtraction of all sources individually detected above 3.7σ. The spatial scale is in arcseconds relative to the expected nominal center of the stacked beam. Contours are shown at 3, 6, 9 times the full stack noise of 0.044 mJy. The gray scale of the images runs from zero to the respective peak.

a few cases with poor statistics we explicitly discuss the effects of significant detections for the stacked population. Given the noticeable overlap between the submillimeter population and weak X-ray sources representing moderate luminosity AGNs (e.g., Alexander et al. 2003, 2005b), exclusion of individually detected submillimeter sources would bias our results. Future detailed identification campaigns and high spatial resolution submillimeter follow-up of the LABOCA survey will allow supplementation of this statistical approach with one based on the confirmed nature of individual sources.

We quote below the stacked fluxes for various samples of ECDFS AGNs. In assigning errors we consider that, while the instrument noise is Gaussian to good approximation (Weiß et al. 2009), the pixel histogram of the LABOCA map is somewhat non-Gaussian due to the effect of individually detected, as well as fainter, sources (Figure 1). Positive detections in stacks are hence more likely than for purely Gaussian noise. We provide in Tables 1 and 2 two error measures for the mean flux of each stack. For a sample with N sources, the error σ_{map} provides the standard deviation from comparing the mean fluxes of many (>1000) samples of N sources each, drawn at random spatial positions in the map. The value of σ_{map} allows assessment of the significance of a stack's detection. The error $\sigma_{subsample}$ provides the standard deviation from comparing the mean fluxes of many subsamples of N sources each, drawn randomly from the fluxes measured at the positions of our combined sample of 895 AGNs. This error is larger than σ_{map} since it also includes the spread in the properties of the AGN population. For that reason, we use it when assessing the significance of differences between subsamples of our overall AGN sample. We have also compared $\sigma_{subsample}$ to error estimates from bootstrapping into each subsample proper and found the latter estimates broadly consistent, but with large fluctuations due to the sometimes small subsamples that are used below.
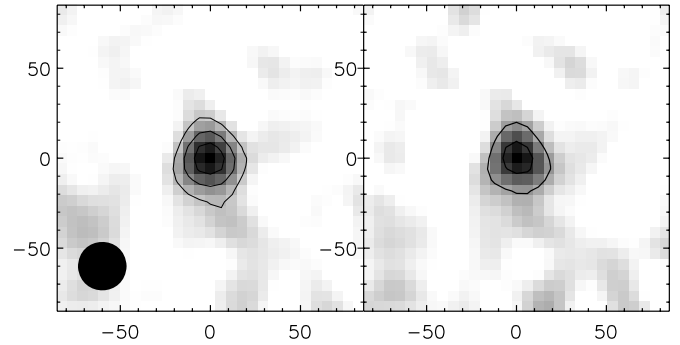
2.3. Stacking Results for Different AGN Samples

The stacked flux for the 895 X-ray sources from the combined CDFS+ECDFS sample is detected clearly at $S_{870\,\mu m} = 0.49 \pm 0.044$ mJy (11.1σ). The stacked image is shown in Figure 2. A two-dimensional Gaussian fit to the stacked beam is centered at $2\rlap{.}''2 \pm 1\rlap{.}''7$ from the expected position and has a Gaussian fit FWHM of 27″ × 34″ (±3″). These parameters support the correctness of the map reduction and the stacking procedure, given the nominal convolved beam of 27″. Stacking the residual map after removal of all $>3.7\sigma$ LABOCA point sources again provides a clear detection at ∼70% of this flux (Figure 2, Table 1). Use of the residual map will lower the average flux of a stacked X-ray population by excluding members of that X-ray population that are individually detected SMGs. It can also lower the average flux if a subtracted point source is dominated by an unrelated object but includes a weaker submillimeter flux that is originating from the blended X-ray source proper. Then, the flux at the position of the nearby X-ray source will be oversubtracted by removing a point source with the combined flux. This is related to one part of the "boosting" effect on the fluxes of low-S/N source detections from such a map. This is avoided for our residual map in a statistical sense because "deboosted" (Coppin et al. 2005) fluxes for the detections have been used when deriving the residue (see also Weiß et al. 2009).

For redshift $z \sim 1$, close to the median redshift of (E)CDFS AGNs, and adopting a $T = 35$ K, $\beta = 1.5$ graybody far-infrared continuum shape for the star formation powered part of the SED, the total infrared luminosity corresponding to our 0.49 mJy LABOCA detection is ∼$2.6 \times 10^{11} L_\odot$. The inferred mean SFR is ∼27 $M_\odot$ yr^{-1}, assuming star formation dominated submillimeter emission, the conversion of Kennicutt (1998) and then multiplying by 0.6 to convert to a Chabrier (2003) initial mass function. Note that for $z > 0.5$ and given the negative K correction for submillimeter emission (e.g., Figure 4 of Blain et al. 2002), the considerable uncertainty of this estimate is mostly in the adopted temperature of dust heated by star formation (Factor $\lesssim 2$ in luminosity for a 5 K difference), rather than in the difference between individual source redshifts and the redshift $z = 1$ adopted for the conversion. The average deep X-ray field AGN is thus residing in a moderately actively star-forming object, its luminosity placing it in the category usually called luminous infrared galaxies

Table 1
Stacking Results for Combined CDFS+ECDFS List

Group	N_{Source}	$S_{870\,\mu\text{m}}$ (mJy)	σ_{map} (mJy)	$\sigma_{\text{subsample}}$ (mJy)	$S_{870\,\mu\text{m,residual}}$ (mJy)	L_{IR} ($10^{11}\,L_\odot$)
(1)	(2)	(3)	(4)	(5)	(6)	(7)
No grouping						
All CDFS & ECDFS	895	0.490	0.044	0.054	0.344	
Grouping by redshift						
$z \leqslant 1.2$	383	0.279	0.066	0.083	0.218	1.15
$z > 1.2$	365	0.637	0.068	0.085	0.445	3.97
$z > 2$	158	0.597	0.106	0.129	0.430	3.79
All z	748	0.453	0.047	0.059	0.328	2.48
No good phot/spec z	147	0.695	0.108	0.134	0.434	

Notes. Column 1: group of X-ray AGN entering the stack. Column 2: number of sources in stack. Column 3: weighted mean of 870 μm flux densities for stack. Measurements for stacks which are at $< 3\sigma$, hence not significantly detected, are highlighted by italics. Column 4: standard deviation of the weighted means, obtained by drawing many samples of N_{Source} at random positions from the LABOCA map. Column 5: standard deviation of the weighted means from drawing many subsamples of N_{Source} from the full $N = 895$ AGN sample. Column 6: weighted mean of 870 μm flux densities for stack on the residual map, obtained by subtracting all individual detections from the original map. For the stacks from the residual map, the corresponding errors σ_{map} and $\sigma_{\text{subsample}}$ (not shown) are consistent with each other and ~12% less than σ_{map} for the full map. Column 7: stacked IR luminosity, from the weighted mean of the luminosities of rest-frame $T = 35$ K $\beta = 1.5$ graybodies individually matched to the redshift and 870 μm flux of each X-ray AGN. Available only for samples with redshifts for each object.

(LIRGs). This result certainly averages over a range of far-infrared luminosities but the LABOCA detection also in the stacked residual map argues that it is not only due to a few luminous outliers. Better characterizing this spread will be a task for the *Herschel Space Observatory*, the ~10 mJy far-infrared SED peak expected for the adopted graybody is well within its capabilities. Given the $>11\sigma$ detection of the combined sample, stacks for subgroups can still be detectable at good significance. We use such substacks in the following to probe for trends with AGN properties.

We start with a simple splitting of the combined sample by redshift (see Table 1 for results of this and subsequent splittings of the combined sample). More than 80% of the sample have redshifts and are split into about equal groups below and above redshift $z = 1.2$. There appears to be a trend toward higher SFRs at higher redshift. A difference in mean submillimeter flux between $z < 1.2$ and $z > 1.2$ sources is found at the 3.0σ level. As for other comparisons of AGN subsamples, we have adopted here the $\sigma_{\text{subsample}}$ errors from Tables 1 and 2. Comparing $z < 1.2$ to $z > 2$ sources gives a similar difference but only at the 2.1σ level, due to the smaller size of the latter group. The sources without redshift assignment on average have slightly higher submillimeter flux than any of these groups, consistent with the notion that a significant fraction of them are located at high redshift and remain more difficult to identify (Alexander et al. 2001; Mainieri et al. 2005b). We can also scrutinize this trend with redshift via a Spearman rank correlation test of the 746 individual submillimeter fluxes with redshift measurements, rather than looking at binned averages. The correlation coefficient is a modest 0.108, not surprising given the significant noise on each individual flux measurement, but the probability of exceeding this coefficient in the null hypothesis of uncorrelated data is only 0.003. Interpreting trends of submillimeter flux with redshift in terms of total infrared luminosity assumes their proportionality due to the negative K-correction. This assumption starts to fail at $z \lesssim 0.5$. However, changes in the ratio of submillimeter flux and inferred infrared luminosity are small at the median redshifts of the bins discussed here (Figure 3). Deviations at $z < 0.5$ act in the direction of strengthening the trend of luminosity with redshift compared to the trend for submillimeter flux. We illustrate this by reporting for those samples in Table 1 with complete redshifts also stacked IR luminosities, obtained from the luminosities of fiducial $T = 35$ K, $\beta = 1.5$ graybodies matched to redshift and submillimeter flux of each source. These stacked luminosities (see also the lower panel of Figure 3) thus capture the effect of the redshift distribution of the samples, and confirm its impact to be small. Results from analyzing redshift subgroups for the CDFS sample only, with its more complete identification status (see Table 2 for this and other results for this sample), agree with results for the combined sample in showing higher flux at higher redshift but with $< 2\sigma$ significance of the trends at the given sample sizes. Of course, the trends with redshift (see also Figure 3) do not immediately imply evolution, because of the luminosity versus redshift selection effects of the underlying X-ray surveys which are effectively flux limited.

To test this further, trends with X-ray luminosity need to be explored. Roughly half of those sources in the combined sample with redshifts are not used here, because of the lack of X-ray spectral modeling for many of the ECDFS-only sources. For them, only a simple observed X-ray luminosity can be computed from the distance and observed X-ray fluxes. No significant trends of average submillimeter flux can be observed with this observed X-ray luminosity, but this could also be due to the effect of variations in the obscuring column density erasing trends with intrinsic AGN luminosity. This aspect is better addressed using only the CDFS sample, for which the spectral fits of Tozzi et al. (2006) assign an intrinsic rest-frame hard X-ray (2–10 keV) luminosity for all sources including hard/obscured ones. We find no noticeable differences between

Table 2
Stacking Results for Tozzi et al. CDFS List

Group	N_{Source}	$S_{870\,\mu m}$ (mJy)	σ_{map} (mJy)	$\sigma_{\text{subsample}}$ (mJy)	$S_{870\,\mu m,\text{residual}}$ (mJy)	L_{IR} $(10^{11}\,L_\odot)$
(1)	(2)	(3)	(4)	(5)	(6)	(7)
No grouping						
All CDFS	302	0.437	0.074	0.094	0.328	2.32
Grouping by redshift						
$z \leqslant 1$	145	0.362	0.109	0.134	0.258	1.47
$z > 1$	157	0.506	0.104	0.128	0.394	3.13
$z > 2$	63	0.779	0.162	0.202	0.561	4.93
Grouping by intrinsic rest-frame 2–10 keV luminosity						
$L < 10^{42}$ erg s^{-1}	48	*0.379*	0.189	0.233	0.289	1.05
$L < 10^{43}$ erg s^{-1}	138	0.361	0.111	0.138	0.305	1.52
$L \geqslant 10^{43}$ erg s^{-1}	164	0.500	0.102	0.126	0.348	3.01
$L < 10^{44}$ erg s^{-1}	260	0.341	0.086	0.101	0.266	1.71
$L \geqslant 10^{44}$ erg s^{-1}	42	1.036	0.200	0.250	0.718	6.24
Grouping by X-ray obscuring column from spectral fit						
$N_{\text{H}} < 10^{22}$ cm^{-2}	114	*0.315*	0.122	0.152	0.280	1.32
$N_{\text{H}} \geqslant 10^{22}$ cm^{-2}	188	0.511	0.095	0.120	0.357	2.94
$N_{\text{H}} < 3 \times 10^{22}$ cm^{-2}	169	0.421	0.098	0.115	0.325	2.04
$N_{\text{H}} \geqslant 3^{22}$ cm^{-2}	133	0.458	0.113	0.140	0.333	2.66
$N_{\text{H}} < 10^{23}$ cm^{-2}	225	0.416	0.087	0.108	0.310	2.08
$N_{\text{H}} \geqslant 10^{23}$ cm^{-2}	77	0.498	0.149	0.123	0.383	3.01
Sources with $L_{2-10\,\text{keV}} \geqslant 3\ 10^{43}$ erg s^{-1}, grouping by X-ray column						
$N_{\text{H}} < 10^{22}$ cm^{-2}	18	*0.072*	0.316	0.378	0.185	0.40
$N_{\text{H}} \geqslant 10^{22}$ cm^{-2}	80	0.641	0.147	0.180	0.427	3.95
$N_{\text{H}} < 10^{23}$ cm^{-2}	48	*0.400*	0.189	0.233	0.341	2.42
$N_{\text{H}} \geqslant 10^{23}$ cm^{-2}	50	0.667	0.184	0.226	0.422	4.12
Sources with $L_{2-10\,\text{keV}} \geqslant 1\ 10^{44}$ erg s^{-1} and spectroscopic redshift, grouping by X-ray column						
$N_{\text{H}} < 10^{22}$ cm^{-2}	6	*0.433*	0.531	0.653	0.549	2.23
$N_{\text{H}} \geqslant 10^{22}$ cm^{-2}	21	1.390	0.285	0.352	0.858	8.43
$N_{\text{H}} < 10^{23}$ cm^{-2}	13	1.098	0.366	0.447	0.860	6.40
$N_{\text{H}} \geqslant 10^{23}$ cm^{-2}	14	1.244	0.346	0.432	0.719	7.57
Sources with $L_{2-10\,\text{keV}} < 3 \times 10^{43}$ erg s^{-1} and spectroscopic redshift, grouping by X-ray column						
$N_{\text{H}} < 10^{22}$ cm^{-2}	96	*0.360*	0.133	0.166	0.298	1.47
$N_{\text{H}} \geqslant 10^{22}$ cm^{-2}	108	0.415	0.124	0.156	0.307	2.23
Sources with $L_{0.5-2\,\text{keV}}$ or $L_{2-10\,\text{keV}} \geqslant 1\ 10^{44}$ erg s^{-1} and spectroscopic redshift, grouping by optical spectral type						
Type 1 (BLAGN)	10	*0.737*	0.410	0.508	0.743	4.29
Type 2	17	1.436	0.315	0.388	0.815	8.64

Notes. Definition of columns as in Table 1. Stacks measured at $< 3\sigma$, hence not significantly detected, are highlighted by italics.

groups or with respect to the total sample when dividing at $L_{2-10\,\text{keV}} = 10^{43}$ erg s^{-1} into a more and a less luminous group with about half of the sample each (Table 2, Figure 4). This changes at the most luminous end: sources with $L_{2-10\,\text{keV}} > 10^{44}$ erg s^{-1} have more than twice the average submillimeter flux, and differ from the average of the CDFS sample at 2.2σ and from the sources with $L_{2-10\,\text{keV}} < 10^{44}$ erg s^{-1} at 2.6σ. We further discuss this stronger star formation around the most luminous X-ray AGNs below. Again the behavior implied by the analysis of the stacks can be tested via a rank correlation of individual submillimeter fluxes with $\log(L_{2-10\,\text{keV}})$. Given the upturn in submillimeter only at the high X-ray luminosity end (Figure 4) it is not surprising that no significant correlation is seen over the full range ($N = 302$, C.C. $= 0.059$, Significance 0.30), but correlation between submillimeter flux and luminosity is found above $L_{2-10\,\text{keV}} > 10^{43.5}$ erg s^{-1} ($N = 98$, C.C. $= 0.26$, significance 0.01).

One of the most interesting parameters that is potentially linked by evolution to the level of star formation is the X-ray obscuring column density. Simple tests that can be done on the combined sample show no trend: binning directly by X-ray hardness ratio as well as by crude estimates of the obscuring column density from the location in the redshift versus hardness ratio diagram (e.g., Figure 8 of Szokoly et al. 2004) does not show any noteworthy changes. We hence focus again on the CDFS sample using the modeled X-ray obscuring column densities N_{H} from Tozzi et al. (2006). As Table 2 and Figure 5 show, there is no significant variation with obscuring column density even for this well-characterized sample and comparing subsamples that are individually detected at 3σ–5σ. We here split the sample at two different column densities. First, $N_{\text{H}} = 10^{22}$ cm^{-2} is often used as the limit distinguishing unobscured AGNs from the larger number of obscured AGNs (e.g., Tozzi et al. 2006). As a second test, we broke the sample at
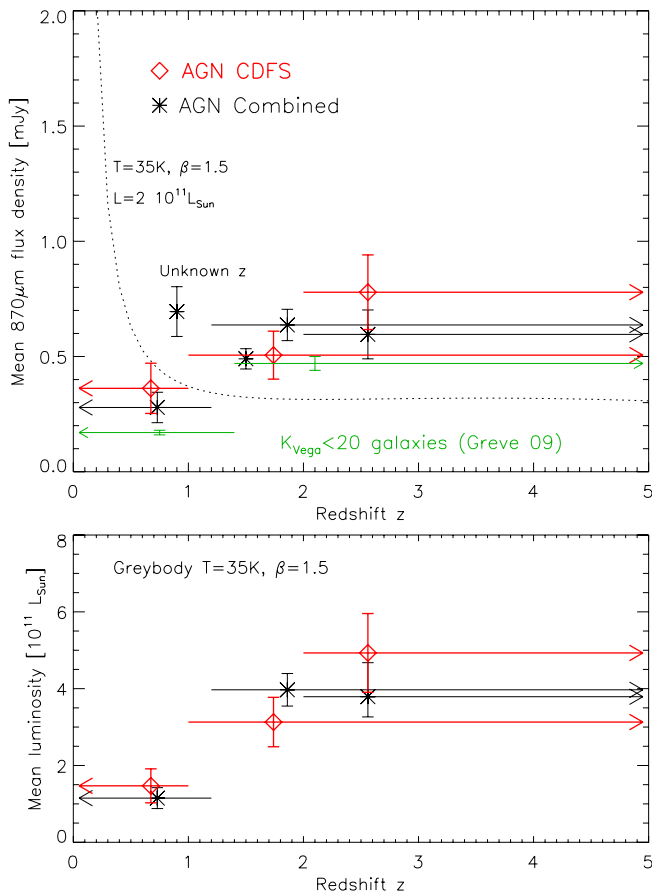
Figure 3. Top panel: X-ray-selected AGNs from the CDFS and ECDFS show an increasing trend of mean submillimeter flux density with redshift. As in similar diagrams below, horizontal bars or arrows indicate the parameter range covered by a subsample, while vertical error bars indicate the 1σ errors of the mean flux for this subsample. The symbols are placed at the median of the quantity on the abscissa for the respective bin—here redshift. The asterisk without redshift range indicates the mean flux of the entire combined sample. Results are shown separately for CDFS AGN only, and for the combined sample of CDFS and ECDFS AGNs. Results for ECDFS sources without reliable redshift are shown at an arbitrary z, most likely these contain a significant fraction of presently unidentified high-redshift sources. The mean submillimeter fluxes of (predominantly non-AGN) $K < 20$ galaxies are added for comparison (Greve et al. 2009, also based on LABOCA data). We also illustrate the submillimeter flux expected from a graybody of given luminosity at different redshifts (dashed curve). Bottom panel: results from stacking the IR luminosities of graybodies fitted to the redshift and map flux of each source.

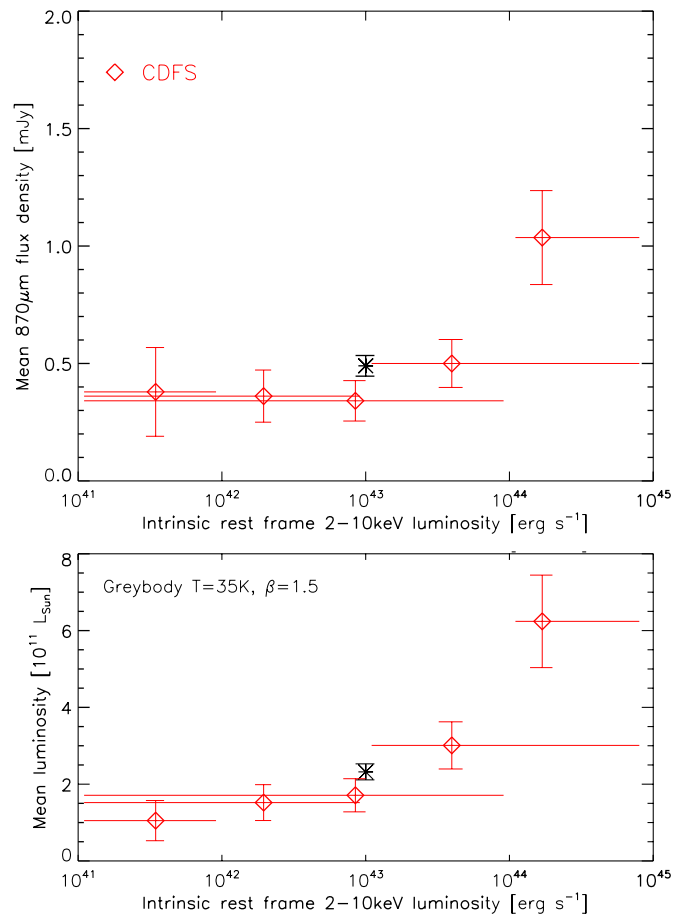(A color version of this figure is available in the online journal.)

Figure 4. Top panel: mean submillimeter flux density as a function of intrinsic rest-frame 2–10 keV luminosity of the AGNs. The asterisk indicates the mean submillimeter flux of the entire combined sample. The mean submillimeter flux rises clearly above $L_{2-10\,\mathrm{keV}} = 10^{44}\,\mathrm{erg\,s^{-1}}$. These highest luminosities are also the sole driver of the flux increase in the wider $L_{2-10\,\mathrm{keV}} = 10^{43}\,\mathrm{erg\,s^{-1}}$ bin. Bottom panel: results from stacking the IR luminosities of graybodies fitted to the redshift and map flux of each source.

(A color version of this figure is available in the online journal.)

2.4. Results for the Most Luminous CDFS X-ray AGNs

In the previous section, we have found for the full population of (E)CDFS X-ray AGNs a trend of submillimeter flux and SFR with redshift, a change with intrinsic X-ray luminosity only at the highest $L_{2-10\,\mathrm{keV}} \geqslant 10^{44}\,\mathrm{erg\,s^{-1}}$ AGN luminosities, the border that is conventionally adopted between "AGN" and "QSO," and no significant change with X-ray obscuring column density. We will discuss the implications below but first specifically repeat the check for possible trends with obscuration at the highest AGN luminosities. This is motivated by the large range of luminosities covered, combined with the possibility that evolutionary paths may significantly differ between luminous QSOs and lower luminosity AGNs.

We first restrict the stacks which are formed via the Tozzi et al. (2006) obscuring column densities to AGNs with high intrinsic luminosity $L_{2-10\,\mathrm{keV}} \geqslant 3 \times 10^{43}\,\mathrm{erg\,s^{-1}}$. A column density $N_{\mathrm{H}} = 10^{23}\,\mathrm{cm^{-2}}$ divides the sample roughly into half, but we also explore the traditional $N_{\mathrm{H}} = 10^{22}\,\mathrm{cm^{-2}}$ separation. In both cases, the more obscured sources appear brighter in the submillimeter (Table 2), but the difference stays well below 2σ significance in either case. As a next step toward the most luminous and reliable sources we further restrict to $L_{2-10\,\mathrm{keV}} \geqslant 10^{44}\,\mathrm{erg\,s^{-1}}$ and sources with spectroscopic

$N_{\mathrm{H}} = 10^{23}\,\mathrm{cm^{-2}}$ which would help identifying changes for the highest column density objects. These two cuts, as well as an intermediate one at $N_{\mathrm{H}} = 3 \times 10^{22}\,\mathrm{cm^{-2}}$ that gives roughly equally populated bins above and below the threshold, do not reveal any significant trends with X-ray obscuring column density. For the $N_{\mathrm{H}} = 3 \times 10^{22}\,\mathrm{cm^{-2}}$ cut which has the most equally distributed statistics, the ratio of stacked submillimeter fluxes for sources more/less obscured than the cut is 1.1 ± 0.5, well below high ratios like the factor 4.4 found in the Stevens et al. (2005) comparison of obscured and unobscured very luminous QSOs. Using submillimeter emission as star formation indicator, there hence seems to be no clear trend of host star formation with nuclear obscuration for the typical $L_{2-10\,\mathrm{keV}} \sim 10^{43}\,\mathrm{erg\,s^{-1}}$ AGN. Recent attempts using radio continuum emission (Rovilos et al. 2007) and the [O II]λ3727 emission line (Silverman et al. 2009) to trace star formation agree in not finding such trends.

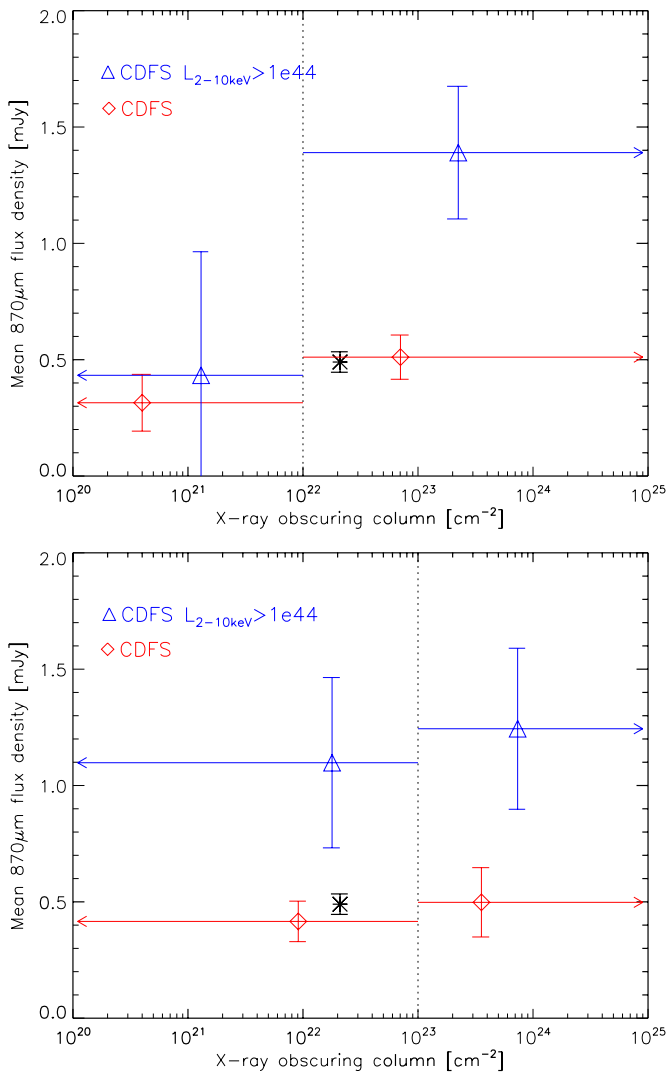**Figure 5.** Trends of mean submillimeter flux density with AGN X-ray obscuring column density. Top panel: sample split at $N_H = 10^{22}$ cm^{-2}, as indicated by the dotted line. Bottom panel: Sample split at $N_H = 10^{23}$ cm^{-2}. The asterisk shows the mean flux of the entire combined sample. We show results for the full CDFS sample, with no indication for a trend with N_H, and for the the most X-ray luminous CDFS sources with good redshifts. From the top panel, these may be more submillimeter luminous above $N_H = 10^{22}$ cm^{-2} compared to below, but the difference is not significant in our sample.

(A color version of this figure is available in the online journal.)

redshifts (redshift quality flag $\geqslant 1$ in Tozzi et al. 2006). Again we find the more obscured sources to be submillimeter brighter (Table 2, Figure 5) with again a larger difference in submillimeter flux if separating at $N_H = 10^{22}$ cm^{-2}, but low significance. Such a change in mean star-forming rate with obscuring column density occurring at roughly $N_H = 10^{22}$ cm^{-2} might indicate that the small variations with column density for the full CDFS sample may be dominated by the contribution of luminous AGN. Consistent with this interpretation, a test splitting the less luminous $L_{2-10\,keV} < 3 \times 10^{43}$ erg s^{-1} AGNs at $N_H = 10^{22}$ cm^{-2} further reduces the difference in submillimeter flux between the two bins, compared to the full sample (Table 2).

An independent way of distinguishing unobscured from obscured AGNs is the optical spectral classification. We use the highest luminosity AGN from Tozzi et al. (2006), for which either $L_{0.5-2\,keV}$ or $L_{2-10\,keV}$ is at least 10^{44} erg s^{-1}. Among those, we restrict ourselves to sources with spectroscopic

redshift (redshift quality flag $\geqslant 1$ in Tozzi et al. 2006) and group them into optical Type 1 (BLAGN in the scheme of Szokoly et al. 2004, 10 sources[15]) or Type 2 (HEX, LEX, or ABS classifications in the scheme of Szokoly et al. 2004, 17 sources[16]). Here we included XID 35 that was not classified by Szokoly et al. (2004) but for which an optical spectrum from the VVDS survey (Le Fevre et al. 2004) is lacking obvious broad lines. Consistent with the analysis where obscuration was defined via the X-ray obscuring column density, the obscured optical Type 2 AGNs are again submillimeter brighter (Table 2) than the unobscured Type 1 AGNs, but the significance of the difference is low at just 1σ.

For both methods, the difference between submillimeter fluxes of luminous unobscured and obscured AGNs is stronger when stacking the flux map compared to stacking the residual map, suggesting a contribution of individually detected submillimeter galaxies. Inspection shows that the "hard" group defined by $N_H > 10^{22}$ cm^{-2} or by optical Type 2 in both cases includes two X-ray sources with S/N in the submillimeter map above 3 at their position, because they are close to submillimeter sources that are detected at $> 3.7\sigma$. Both have extracted submillimeter fluxes of $\gtrsim 6$ mJy. The "soft" group in contrast has no such sources. These two SMGs are near the X-ray sources with Giacconi et al. (2002) XIDs 51 ($z = 1.097$) and 112 ($z = 2.940$). We have investigated these associations on the LABOCA map, the VLA data of Miller et al. (2008) and the FIDEL 24 μm image (M. Dickinson et al. 2010, in preparation). For XID 112, the position of the optical identification for which Szokoly et al. (2004) determined the redshift agrees within $1''$ with a weak $S_{1.4\,GHz} = 48\,\mu$Jy radio source and a 24 μm source, and is only $2''.4$ from SMG LESS J33152.0−275329 (Weiß et al. 2009). This supports the association despite the fact this is a relatively complex region of the LABOCA map with two more submillimeter sources within less than 1 arcmin. For XID 52, again the optical position agrees with a (93 μJy) radio source and a 24 μm source, but the offset to LESS J33217.6−275230 is $10''.8$, large ($\gtrsim 2\sigma$) for identifications of such a $\sim 5\sigma$ submillimeter detection and the $27''$ convolved LABOCA beam (e.g., Equation (B22) of Ivison et al. 2007) and the $6''$ positional accuracy estimated for the LABOCA map in Weiß et al. 2009). We maintain this source in our stacks given that there is no nearby alternative radio identification for the SMG, and the region is again complex with the next SMG detection almost blended, but this association is clearly uncertain.

In our comparison of obscured and unobscured $L_{2-10\,keV} > 10^{44}$ erg s^{-1} AGNs, we have found brighter submillimeter fluxes by a factor ~ 3 comparing X-ray column densities above to below $N_H = 10^{22}$ cm^{-2} and by a factor ~ 2 comparing optical Type 2 to Type 1. This is intriguing but the significance of the differences is too low in either case to claim a detection from our sample. The next steps in sample and field size and/ or errors on the individual star-forming rates will be needed for robustly confirming whether the stronger star formation reported at higher AGN luminosity in X-ray obscured versus unobscured broad-line AGNs (Page et al. 2001, and subsequent work) also holds in the regime of the brightest X-ray sources found in deep surveys like the (E)CDFS.

---

[15] Giacconi et al. (2002) XIDs 11, 22, 24, 42, 60, 62, 67, 68, 91, 206.
[16] Giacconi et al. (2002) XIDs 18, 27, 31, 35, 45, 51, 57, 76, 112, 153, 156, 202, 253 (changed redshift from Szokoly et al. 2004 in Tozzi et al. 2006, see also Roche et al. 2006), 263, 268, 547, 601.

2.5. Results on Individual Literature X-ray Sources

CXOCDFS J033229.9−275106 (also called CDFS-202; Norman et al. 2002) at redshift of $z = 3.70$ has been considered a prototype of a luminous radio-quiet X-ray-selected type 2 QSO. Sturm et al. (2006) have obtained a deep *Spitzer* mid-infrared spectrum of this source, detecting the AGN continuum but not the 6.2 μm rest wavelength PAH emission feature that could be detectable at this depth if the source were also hosting an extremely luminous SMG-like starburst. In accordance with this result, the LABOCA map does not show a detection at the position of CDF-S 202 ($S_{870} = -1.01 \pm 1.10$ mJy).

From deep SCUBA follow-up of four heavily X-ray absorbed and X-ray luminous AGNs in the CDFS, Mainieri et al. (2005a) report a $S_{850} = 4.8 \pm 1.1$ mJy detection for the $z = 3.66$ object CDFS-263. The LABOCA map gives a flux of $S_{870} = 1.88 \pm 1.16$ mJy for this source. While we cannot support the Mainieri et al. (2005a) result by an independent significant detection, the two measurements are still consistent within 2σ given the errors, and the source is likely among the submillimeter brighter part of the X-ray AGN population. Rigopoulou et al. (2009) publish results from an extension of this project to eight sources. They do not detect at 850 μm CXOCDFS J033229.9−275106, consistent with the LABOCA and *Spitzer* results reported for this source above. Stacking their eight targets in the LABOCA map we find $S_{870} = 1.55 \pm 0.41$ mJy, consistent with results for $L_{2-10\,\mathrm{keV}} > 10^{44}$ erg s^{-1} Type 2 AGN reported above but somewhat lower than the $S_{870} = 4.0 \pm 0.5$ mJy obtained from scaling the variance-weighted mean of the Rigopoulou et al. (2009) SCUBA results to 870 μm.

Koekemoer et al. (2004) report the detection in the GOODS-S region of 7 extreme X-ray/optical ratio sources (EXOs) characterized by robust *Chandra* X-ray detections but optical nondetections to extremely low limits. All of these fall on the LABOCA map, none of them is individually detected and the stacked flux is 0.07 ± 0.43 mJy. While this nondetection at submillimeter wavelengths excludes an explanation of EXOs by obscured AGNs that are co-existent with extreme star formation, it is compatible with other possible SEDs of AGNs at moderate to extremely high redshifts.

3. DISCUSSION

Our data put strong limits on possible trends in submillimeter brightness with obscuration for AGNs with moderate luminosities, but are consistent with such a trend for luminous AGNs. This result can be compared to previous studies. The first comparisons of deep X-ray and submillimeter surveys mentioned in the introduction had too limited statistics to reliably address this issue. Page et al. (2001) used a different approach of selecting very luminous hard X-ray sources from the *ROSAT* survey and obtained significant submillimeter detections in four out of eight $z = 1$–2.8 obscured AGNs, the weighted mean submillimeter flux for all eight is $S_{850} = 4.4 \pm 0.5$ mJy. Subsequent papers (Page et al. 2004; Stevens et al. 2005) supported this result by matching to unobscured AGNs of similar luminosity and redshift, and by extension of the sample size, overall finding a ratio 4.4 in submillimeter flux between X-ray unobscured and obscured AGNs, and with the difference between submillimeter detection rates of individual objects in the two groups significant at the 3σ–4σ level.

Our LABOCA results grouping luminous ($L_{2-10\,\mathrm{keV}} > 10^{44}$ erg s^{-1}) CDFS X-ray AGN by obscuration provide a ratio 2–3 in submillimeter flux between obscured and unobscured

objects, using separations by either $N_H = 10^{22}$ cm^{-2} or by optical spectral type. However, due to the low significance we cannot rule out neither absence of a difference nor trends as reported by Page et al. (2001) and subsequent papers. One should note that, considering the $\sim$8% correction from 870 μm to 850 μm flux densities for $\beta = 1.5$ optically thin dust at $z = 1$–4, our average submillimeter fluxes of obscured sources are a factor $\sim$2–3 lower than reported by Page et al. (2001) and Stevens et al. (2005) for their samples. Assuming that the increase of submillimeter flux with X-ray luminosity at highest luminosities (Figure 4) continues beyond the range up to $L_{2-10\,\mathrm{keV}} \sim 8 \times 10^{44}$ erg s^{-1} covered by our sample, this difference may be due to the typically higher $L_{2-10\,\mathrm{keV}} \sim 10^{45}$ erg s^{-1} luminosities of the Stevens et al. (2005) sample (see also Figure 6). Observations with better statistics at $L_{2-10\,\mathrm{keV}} \gtrsim 10^{44}$ erg s^{-1} will be needed to firmly establish whether in this regime not only the observed increase in submillimeter flux occurs, but also a gap starts to open between submillimeter properties of unobscured and obscured AGNs.

An important point to note is that the Stevens et al. (2005) obscured QSOs are X-ray absorbed (though with typical N_H just above 10^{22} cm^{-2} not Compton thick) but optical broad-line region (Type 1) objects. Stevens et al. are comparing optical Type 1 QSOs having low X-ray absorbing column density with Type 1 but higher X-ray absorbing column density. In contrast, we were first comparing groups defined by X-ray column density only, and in the second test comparing optical Type 1 to optical Type 2. Splitting our very small sample of 10 X-ray luminous BLAGN further by X-ray column density to fully reproduce the Stevens et al. (2005) approach did not show significant differences of subgroups in this group. While our result is consistent with the Stevens et al. (2005) finding of increased submillimeter flux for obscured luminous AGNs, the detailed role of different definitions of AGN obscuration remains to be investigated with better sensitivity and statistics.

Sturm et al. (2006) used *Spitzer* mid-infrared spectroscopy to detect or put limits on star formation in a sample of eight optical type 2 QSOs selected from deep X-ray surveys. These objects span a range of intrinsic luminosities $L_{0.5-10\,\mathrm{keV}} = 10^{43.1}$ to 10^{45} erg s^{-1} and X-ray obscuring column densities $N_H = 10^{21.3}$ to $>10^{24}$ cm^{-2}, with all but one above 10^{22} cm^{-2}. We discussed the consistent LABOCA results for the $z \sim 3.7$ source CDFS-202 above. For the major part of their sample, six sources at redshifts 0.205 to 1.38 (median $\sim$0.5), Sturm et al. (2006) report one detection and five limits on mid-infrared PAH emission with inferred star-forming luminosities of the order 2×10^{10} $L_\odot$. This is lower than the $\sim$1.1 $\times 10^{11}$ $L_\odot$ obtained from the mean LABOCA flux for the $z < 1.2$ redshift bin, averaging over all X-ray luminosities (Figure 3), converting via our adopted $T = 35$ K, $\beta = 1.5$ SED and assuming $z = 0.6$. The Sturm et al. (2006) sample is small and may have missed star-forming objects, but another factor likely contributing to the difference is the extrapolation from the PAH measurements to total star-forming luminosity which is a function of interstellar medium conditions. Sturm et al. (2006) adopted a scaling factor based on the star-forming galaxy M82. A scaling factor more similar to the one for high radiation field intensity environments, as suggested for star formation in hosts of local type 1 QSOs by Schweitzer et al. (2006), would increase the inferred SFRs/limits of Sturm et al. (2006) by a factor $\sim$4 and bring them close to the typical $z < 1$ SFR inferred from the LABOCA submillimeter fluxes.
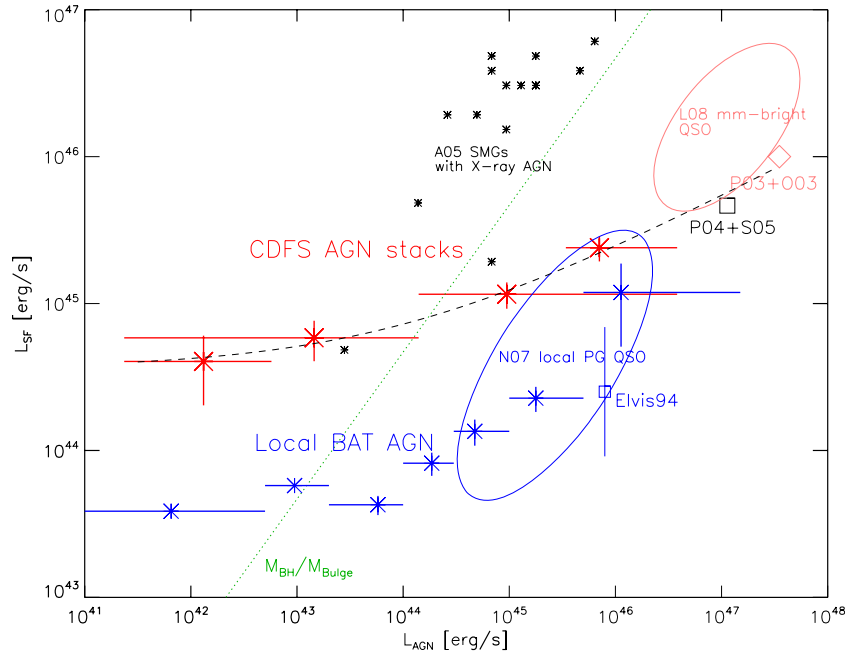
Figure 6. AGN luminosities and star-forming far-infrared luminosities for high-redshift and local AGNs. Moderate luminosity AGNs have host star formation rather independent of AGN luminosity, but at a level rising with redshift. For high AGN luminosity, AGN luminosity and host star formation correlate. Red asterisks represent the four CDFS AGN stacks grouped by intrinsic 2–10 keV X-ray luminosity, as also shown in Figure 4 and Table 2. The four stacks are for $L_{2-10\,\mathrm{keV}} < 10^{42}$, $< 10^{43}$, $> 10^{43}$, and $> 10^{44}$ erg s^{-1} (see also the horizontal bars indicating the range of AGN luminosities entering) and are plotted at the median AGN luminosity of the sources in each stack. The diagonal dotted green line indicates the relation for a continuous host and black hole growth, reflecting the local universe relation between black hole mass and bulge mass. The black square represents the combined X-ray obscured and unobscured samples of more luminous X-ray AGN from Page et al. (2004) and Stevens et al. (2005; P04, S05, respectively); see also Section 3. AGN and star formation luminosities have been obtained analogously to the CDFS stacks. The pink ellipse indicates the location in such a diagram of millimeter-bright and optically very luminous high-z QSOs studied by Lutz et al. (2008, L08). The pink diamond reflects the suggested median location of the parent population of these luminous high-z QSOs including millimeter-faint ones, as discussed in Lutz et al. (2008) and based on the surveys of Priddey et al. (2003) and Omont et al. (2003; P03, O03, respectively). The dashed line is a simple constant plus power-law relation between AGN and star-forming luminosity approximating the high-redshift AGNs. We also include local universe ($z < 0.3$) AGNs, the blue ellipse representing local PG QSOs studied by Netzer et al. (2007) and the blue asterisks stacks of local hard X-ray-selected AGN based on *Swift*-BAT and *IRAS* data (Section 3.3). The blue square represents the Elvis et al. (1994) QSO sample at its median AGN luminosity converted to our cosmology, with the error bar indicating the 1σ variation in FIR/optical (star formation/AGN) flux ratio of objects in that sample. Submillimeter galaxies with weak X-ray AGNs (Alexander et al. 2005a) are shown for comparison.

(A color version of this figure is available in the online journal.)

Another modestly sized $z \sim 0.5$ QSO2 sample studied spectroscopically with *Spitzer* was presented by Zakamska et al. (2008). They observed 12 type 2 QSOs, 10 of which were selected from a large area Sloan Digital Sky Survey (SDSS) sample primarily based on their optical Type 2 spectra, large [O III] luminosities, and bright mid-infrared continua. Two sources of their sample of 12 entered the sample from different far-infrared selected programs. Compared to the Sturm et al. QSO2s they exhibit larger AGN mid-IR luminosities and, on the basis of X-ray to [O III] ratios, possibly higher X-ray obscuring column densities. Zakamska et al. report PAH detections in six of 12 objects and infer a typical star formation luminosity of $\sim 5 \times 10^{11}\, L_{\odot}$ from the median of detections and limits. Both of these *Spitzer* spectroscopic studies are broadly consistent with the LIRG-like star-forming luminosities of luminous type 2 AGNs found in our LABOCA study. The overlap in luminosity, redshift, and other properties is not large enough for a direct comparison of methods. A combination into a single analysis is not straightforward, given the different uncertainties that are involved in extrapolation to far-infrared luminosity from either the mid-infrared or submillimeter side.

3.1. The Co-evolution of X-ray Survey AGNs with their Hosts: Two Paths?

The differences expected in the merger evolution scenario between star formation around obscured and unobscured AGNs

may be present only at the high luminosity end of our sample and have been reported by Page et al. (2001) at yet higher luminosities. For the bulk of lower luminosity $L_{2-10\,\mathrm{keV}} \sim 10^{43}$ erg s^{-1} sources we do not observe any significant trend with obscuration. This is likely indicating a different evolutionary path for these AGNs and their hosts.

The host properties of high-redshift Type 1 and luminous Type 2 AGNs are difficult to constrain via common optical/near-infrared techniques, as the AGN often outshines the host. For the more accessible intermediate luminosity and Type 2 part of the population, several studies have concluded that $z \lesssim 1$ X-ray AGNs are hosted by massive galaxies spanning the region from around the top of the "blue cloud" via the "green valley" to the "red sequence" in a color–absolute magnitude diagram (Nandra et al. 2007; Silverman et al. 2008; Treister et al. 2009). These are luminous host galaxies, with few of them fainter than rest-frame absolute magnitude $M_B = -20.5$ and typically brighter than $M_B = -21$ (see also Barger et al. 2003). Photometric stellar mass analyses for $z \sim 1$ X-ray AGN hosts (Alonso-Herrero et al. 2008; Bundy et al. 2008; Lehmer et al. 2008; Silverman et al. 2009) and analogy to the M_B–stellar mass relation for the general $z = 0.7$–1 population (e.g., Cooper et al. 2008) suggests $\log(M*) \gtrsim 10.5\, M_{\odot}$ massive hosts. It is plausible from these results as well as from the local evidence (Kauffmann et al. 2003) to assume that also the bulk of the $z \sim 1$ unobscured/luminous X-ray AGN population resides in massive host galaxies.

Several studies have recently used mainly mid-infrared star formation indicators to conclude that typical massive galaxies at redshifts 0.7–2 are almost constantly forming stars at considerable SFRs, with the stellar mass normalized specific star formation rate (SSFR) increasing with redshift. This is concluded from the presence of a fairly tight mass–SFR relation which shifts toward higher SSFR with redshift (Noeske et al. 2007; Elbaz et al. 2007; Daddi et al. 2007). The tightness of this relation suggests a high duty cycle of star formation. For massive $z \sim 2$ galaxies, a strong role of secular evolutionary processes compared to individual brief merger events is independently suggested by dynamical studies of rest-frame optical/UV selected high-redshift galaxies (e.g., Förster Schreiber et al. 2006; Genzel et al. 2008; Shapiro et al. 2008).

This developing picture of $z \sim 1$–2 galaxy evolution is naturally complemented by our results for the bulk of the X-ray sample: strong trends of host SFR with AGN obscuration are lacking because such SFRs are pervasive in galaxies of similar mass and redshift. The hosts are evolving secularly and star formation is not linked to a specific state of the AGNs. The typical $\sim 30 \, M_\odot \, \mathrm{yr}^{-1}$ estimated above for AGN hosts assuming star formation dominated submillimeter emission compares well with typical SFRs in $z \sim 1 \, \log(M*) \sim 10.5 \, M_\odot$ galaxies (Noeske et al. 2007; Daddi et al. 2007). A further comparative interpretation is currently not warranted given the uncertainty in the stellar masses of the AGN hosts and the fact that the comparison of SFRs is subject to different extrapolation effects. SFRs in these studies are based on extrapolation from the optical/mid-infrared while we extrapolate from the submillimeter. This mismatch can be partly remedied by a comparison to submillimeter fluxes (measuring the rest-frame far-infrared and indirectly SFRs) that were estimated for optically selected galaxies from the LESS LABOCA survey. Greve et al. (2009) find for a K-selected $K_{\mathrm{Vega}} \leqslant 20$ sample stacked 870 μm fluxes of 0.17 ± 0.01 mJy ($z < 1.4$) and 0.47 ± 0.03 mJy ($z > 1.4$), similar but slightly below our trend for the AGN hosts, and again with a positive trend with redshift. The increase in AGN host SFR with redshift (Figure 3) is combined with a relation SFR-to-AGN luminosity that is flat over a wide range of moderate AGN luminosities (Figure 4), i.e., SFR does not depend on AGN luminosity. This is consistent with the moderate luminosity AGN hosts indeed following the increase of SSFR with redshift of the general galaxy population. Firmly establishing this behavior will require studies with better SFR sensitivity for individual objects, removing the need to average over large stacks and better breaking redshift–luminosity correlations in the parent X-ray sample. Silverman et al. (2009) use the AGN-subtracted [O II]λ3727 emission line to compare SFRs in $0.48 < z < 1.02$ AGNs and inactive galaxies of same stellar mass at same redshift. For moderate luminosity $42 < \log(L_{0.5-10\,\mathrm{keV}}) < 43.7$, they find indistinguishable SFR distributions in full agreement with the submillimeter result. When including larger AGN luminosities a SFR excess is indicated in their data. If robust to the increasing technical difficulties of measuring mass and [O II] SFR for luminous AGN, this could indicate the onset of star formation enhancement due to, e.g., merging.

Our interpretation that most of the moderate luminosity X-ray survey AGNs are hosted by massive secularly evolving galaxies is consistent with morphological analyses. *Hubble Space Telescope* (*HST*) studies of $z \sim 1$ X-ray AGN hosts (Grogin et al. 2005; Pierce et al. 2007) find the hosts to typically be bulge-dominated galaxies with only a modest fraction of hosts showing clear morphological evidence for recent major mergers, such as strong asymmetries.

Analysis of deep X-ray surveys has clearly shown a difference in the redshift evolution of high and lower luminosity AGNs, with the comoving density of lower luminosity AGNs peaking at lower redshift than the $z \sim 2$ "Quasar epoch." Since cosmic halo merger evolution can be roughly matched to the evolution of quasars but not to the evolution of lower luminosity AGNs, this has been interpreted in terms of a difference between merger driven accretion at high AGN luminosities and more secular evolution at lower luminosities (e.g., Hasinger 2008; Hopkins & Hernquist 2009, and references therein).

All these lines of evidence place the bulk of the AGN population detected in deep X-ray surveys on a relatively gentle and secular evolutionary path. In these sources, X-ray obscuration may vary through orientation of the immediate AGN environment in a classical unified/torus picture, and possibly also with an additional contribution by obscuration on larger host scales, but obscuration is not intimately linked to the global SFR of the host. Only for the $L_{2-10\,\mathrm{keV}} \gtrsim 10^{44} \, \mathrm{erg \, s}^{-1}$ QSO-like AGNs, obscuration may coincide with high star formation, consistent with a classical merger evolutionary path.

3.2. Star Formation and AGN Accretion Rates

Over cosmic time, the growth and merger rates of black holes and their hosts have to establish the local black hole–bulge mass relation (e.g., Marconi & Hunt 2003; Häring & Rix 2004). In this context, it is interesting to compare for high-redshift AGN populations the current accretion rate onto the black hole and the host growth via star formation with a relation that would establish on average the local ratio of black hole and bulge mass. Our results permit steps in this direction for X-ray-selected AGNs, within the constraints of results that are based on averaging over sizeable samples.

In Figure 6, we show the location of the CDFS stacks, grouped by intrinsic 2–10 keV X-ray luminosity as in Figure 4, now in a diagram comparing star-forming and AGN luminosity. To obtain the AGN luminosities we have converted from median 2–10 keV X-ray luminosity for each luminosity bin, assumed to be AGN dominated, to monochromatic 5100 Å luminosity using the luminosity-dependent α_{OX} relation of Steffen et al. (2006) as cast into units suitable for our purpose by Maiolino et al. (2007). We have then converted to AGN bolometric luminosity adopting $L_{\mathrm{Bol}} = 7\nu L_\nu(5100 \, \text{Å})$ (e.g., Netzer & Trakhtenbrot 2007). The star-forming luminosities are based on the stacked graybody luminosities for an adopted $T = 35$ K, $\beta = 1.5$ SED at the individual redshift of each source. For comparison, we add samples of low- and high-redshift QSOs (Netzer et al. 2007; Lutz et al. 2008; Page et al. 2004; Stevens et al. 2005; Priddey et al. 2003; Omont et al. 2003). The local universe ratio of black hole to bulge mass ratio of 0.14% (Häring & Rix 2004) can be converted into a formal "steady growth luminosity ratio" for star formation and AGN $L_{\mathrm{SF}}/L_{\mathrm{AGN}} = 4.7(0.1/\eta)$ that is shown in Figure 6 for a black hole accretion efficiency $\eta = 0.1$.

The points shown for the CDFS X-ray AGNs reflect the stack averages, i.e., the individual objects may scatter noticeably toward higher and lower SFRs. Nevertheless, their location around the "continuous growth" line is compatible with the picture of secular evolution outlined in the previous section. AGN accretion rates or SFRs may here fluctuate to some extent with time, moving individual sources around this line in Figure 6 in left/right and up/down direction, respectively, but the location of the population overall does not require to place them in any special evolutionary state that would be deviating from a long term growth. Only the highest luminosity

$L_{2-10\,\mathrm{keV}} > 10^{44}\,\mathrm{erg\,s^{-1}}$ CDFS AGNs approach the location of the local and high-redshift QSO in the comparison samples. Compared to the continuous growth ratio, these most luminous X-ray AGNs as well as the QSOs are growing their black holes at a much faster rate, indicating that the matching star formation is most likely spread over longer timescales. Again, we find that only the most luminous CDFS AGNs match the possibly merger related evolutionary pattern of QSOs.

The combination in Figure 6 of the CDFS AGNs with the more luminous high-redshift AGNs observed in the (sub)millimeter by Priddey et al. (2003), Omont et al. (2003), Page et al. (2004), and Stevens et al. (2005) confirms the behavior discussed in Section 2.1. Star formation in the hosts of modest luminosity high-z AGNs seems to depend little on the exact AGN luminosity—reflecting the "secular path." These external samples, however, extend the increase in star formation above $L_{2-10\,\mathrm{keV}} \sim 10^{44}\,\mathrm{erg\,s^{-1}}$ ($L_{\mathrm{AGN}} \sim 3 \times 10^{45}\,\mathrm{erg\,s^{-1}}$) that was already indicated in the CDFS data—reflecting the connection between star formation and AGNs on the "evolutionary connection/merger path." The combined results for these samples and the CDFS AGN can be approximated by a simple relation $L_{\mathrm{SF}} = 10^{44.56} + 10^{27.7} \times L_{\mathrm{AGN}}^{0.38}$ (dashed line in Figure 6). Here, the smaller slope for the power law at high AGN luminosities compared to the slope 1 implied by the "steady growth ratio" plausibly reflects that at the highest AGNs luminosities, the AGN growth (at the time of observation) is increasingly faster compared to the host growth. While this simple two-component constant plus power-law parameterization is a plausible reflection of the two growth modes, it should be considered illustrative and detailed parameters viewed with caution, given the sample selections and the fact that we here compare the $z \sim 1$ AGNs at moderate luminosities and the $z \sim 2$ AGNs at the highest luminosities.

3.3. Comparison to the Local AGN Population

The two evolutionary paths outlined above for high-redshift AGN from deep X-ray fields imply a straightforward consistency check with the local AGN population. If the hosts of moderate luminosity AGNs at $z \sim 1$ have SFRs similar to non-active massive galaxies at the same redshift, the SFRs in the host of moderate luminosity AGNs should follow the decrease of star formation on the general massive galaxy population toward redshift zero.

To perform this check in a methodology as consistent with the LABOCA analysis of (E)CDFS X-ray AGN as possible, we have used a local unbiased 14–150 keV extremely hard X-ray-selected AGN sample from the 39 month Palermo *Swift*-BAT catalog (PSB; Cusumano et al. 2009, see also Tueller et al. 2008 for an earlier BAT AGN catalog) in conjunction with the *IRAS* all-sky far-infrared survey. We selected (L. Shao et al. 2010, in preparation) from the PSB survey sources classified as Seyferts, LINERS, quasars, and other AGNs, explicitly omitting blazars. We excluded remaining objects with the possibility of a strong nonthermal contribution to the far-infrared on the basis of the NED SED, objects at galactic latitude $|b| < 15$ and objects at redshift $z > 0.3$ for which the *IRAS* $60\,\mu\mathrm{m}$ band no longer probes the rest-frame far-infrared. For the remaining 293 AGNs we used the *IRAS* Faint Source Catalog $60\,\mu\mathrm{m}$ detections where available, otherwise we used Scanpi[17] to obtain $60\,\mu\mathrm{m}$ measurements for faint or individually nondetected objects. We calculated rest-frame 2–10 keV luminosities extrapolating

from the BAT fluxes and the redshift, assuming an AGN photon index of 1.8, and infrared luminosities $\nu L_\nu(60\,\mu\mathrm{m})$ in the observed frame. Because about 20% of the sample are individually undetected at $60\,\mu\mathrm{m}$ and for consistency with the LABOCA stacking, we stacked the luminosities in seven 2–10 keV luminosity bins spanning the PSB luminosity range with sufficient statistics in each bin.

Star-forming and AGN luminosities for these local AGN stacks are shown in Figure 6 in direct comparison to the (E)CDFS results. At moderate AGN luminosities ($L_{\mathrm{AGN}} < 3 \times 10^{44}\,\mathrm{erg\,s^{-1}}$), the star-forming luminosities of local hosts are about an order of magnitude lower than in $z \sim 1$ (E)CDFS AGN hosts. On the other hand, these local AGNs appear to follow down to lower AGN luminosities the diagonal correlation of star-forming and AGN luminosity that is reflecting the "merger path." This is in full agreement with previous local work, for example, the infrared-based results of Rowan-Robinson (1995) and Netzer et al. (2007) covering the regime of local QSOs, and modeling based on SDSS spectroscopy by Netzer (2009). The latter traces a correlation down to even lower AGN luminosities $\lesssim 10^{43}\,\mathrm{erg\,s^{-1}}$ where SFRs in our BAT stacks flatten out. We speculate this might relate to a more difficult disentanglement of weak AGN and moderately star-forming galaxies in optical spectra than in very hard-X versus far-infrared.

Mullaney et al. (2010) use *Spitzer* $70\,\mu\mathrm{m}$ data to trace the evolution of the far-infrared to X-ray luminosity ratio of AGNs to redshift $z \sim 2$. They find no significant change of IR luminosity with redshift for luminous $L_{2-10\,\mathrm{keV}} = 10^{43-44}\,\mathrm{erg\,s^{-1}}$ X-ray AGNs but an increase for more modest $L_{2-10\,\mathrm{keV}} = 10^{42-43}\,\mathrm{erg\,s^{-1}}$ AGNs. While an observed wavelength of $70\,\mu\mathrm{m}$ makes for a difficult AGN/host diagnostic at the high-z/high-l end of that range, where AGN-heated dust will enter strongly the observed band, these results agree with our submillimeter-based finding that an increase of host SFR from local toward $z \sim 1$ occurs for modest luminosity AGNs only. We note that the FIR luminosity increase by about an order of magnitude to $z \sim 1$ would be difficult to reconcile with the alternative explanation of an AGN covering factor increase (Mullaney et al. 2010), since covering factors <0.1 would be required for local AGN. Another recent study (Trichas et al. 2009) addresses the starburst/AGN connection in luminous $z \sim 1$ SWIRE AGN. Being based on rare $70\,\mu\mathrm{m}$ detections only it is not directly comparable to our work but consistent with the presence of elevated star formation in $L_{2-10\,\mathrm{keV}} \sim 10^{43}\,\mathrm{erg\,s^{-1}}$ $z \sim$ AGNs.

Our finding of elevated star formation in modest luminosity high-z AGNs is consistent with the change of typical SFRs from $z \sim 1$ to $z = 0$ in the non-active massive galaxy population (Noeske et al. 2007; Elbaz et al. 2007; Daddi et al. 2007). In Figure 6, both local and $z \sim 1$ AGNs are consistent with a "secular" path with star-forming luminosity independent of AGN luminosity, and an "evolutionary connection" path with increasing star-forming luminosity at high AGN luminosity. The evolutionary path, possibly linked to merging, appears to emerge locally at lower AGN luminosities from the locally lower level of general star formation.

We have previously discussed the location of local and high-redshift X-ray-selected AGNs and optical QSOs in the L_{SF} versus L_{AGN} diagram of Figure 6. In the merger evolutionary picture and in a sequence where the strongest star formation occurs before strongest AGN activity, galaxies should follow a loop path moving up in the L_{SF} versus L_{AGN} diagram with the rise of star formation and then to the right and perhaps down toward the most intense AGN phase (see discussion in Netzer

---

[17] http://scanpi.ipac.caltech.edu:9000/applications/Scanpi/index.html

2009). We have placed SMGs *with weak X-ray AGNs* from Alexander et al. (2005a) in Figure 6 to show that their location in comparison to QSOs is consistent with such a path. SMGs without detected AGNs would be found yet further to the left in Figure 6. Comparing the location of individual submillimeter-selected SMGs hosting weak AGNs to the X-ray-selected CDFS stacks has to be done with caution since the CDFS stacks themselves will contain similar SMGs contributing to the upturn in millimeter emission at high X-ray luminosity. A thorough analysis of possible evolutionary loops in such a L_{SF} versus L_{AGN} diagram will thus have to be done on the basis of future individual measurements for sources in all the relevant parts of the diagram.

4. CONCLUSIONS

We have used the combination of the LESS $870\,\mu$m survey and deep X-ray surveys of the (E)CDFS region to study star formation in the hosts of AGNs covering a wide range of redshifts and luminosities centered around $z \sim 1$ and $L_{2-10\,keV} \sim 10^{43}\,erg\,s^{-1}$. Stacking LESS data at the positions of all 895 AGNs we detect at high significance submillimeter emission at $S_{870\,\mu m} = 0.49 \pm 0.04$ mJy corresponding to average SFRs of about $30\,M_\odot\,yr^{-1}$. Using the good statistics to break down the sample according to AGN properties, we find an increase with redshift and little change with AGN luminosity, except for indications for an upturn in host star formation at $L_{2-10\,keV} > 10^{44}\,erg\,s^{-1}$. The bulk of the X-ray AGN does not show changes with AGN obscuration as expected from the merger evolutionary scenario, but such a behavior may emerge at $L_{2-10\,keV} \gtrsim 10^{44}\,erg\,s^{-1}$.

Combined with results for higher luminosity AGNs not properly sampled in the $0.25\,deg^2$ ECDFS, we conclude that the bulk of deep survey X-ray AGNs seems to be hosted by galaxies evolving secularly, with SFRs similar to comparably massive non-active galaxies and no close link between AGNs and global host star formation. In contrast, the most luminous $L_{2-10\,keV} > 10^{44}\,erg\,s^{-1}$ AGNs seem to follow a path where AGN activity and obscuration appear to be more closely linked to host star formation, likely via merger evolution.

The properties of local *Swift*-BAT selected AGN with *IRAS*-based far-infrared star-forming luminosities are consistent with these two paths. The host SFRs of moderate luminosity AGN are decreasing from $z \sim 1$ to $z = 0$ similar to the decrease of SFR in non-active massive galaxies over this redshift interval.

REFERENCES

Alexander, D. M., Bauer, F. E., Chapman, S. C., Smail, I., Blain, A. W., Brandt, W. N., & Ivison, R. J. 2005b, ApJ, 632, 736
Alexander, D. M., Brandt, W. N., Hornschemeier, A. E., Garmire, G. P., Schneider, D. P., Bauer, F. E., & Griffiths, R. E. 2001, AJ, 122, 2156
Alexander, D. M., Smail, I., Bauer, F. E., Chapman, S. C., Blain, A. W., Brandt, W. N., & Ivison, R. J. 2005a, Nature, 434, 738
Alexander, D. M., et al. 2003, AJ, 125, 383
Alexander, D. M., et al. 2008, AJ, 135, 1958
Almaini, O., et al. 2003, MNRAS, 338, 303
Alonso-Herrero, A., Pérez-González, P. G., Rieke, G. H., Alexander, D. M., Rigby, J. R., Papovich, C., Donley, J. L., & Rigopoulou, D. 2008, ApJ, 677, 127
Barger, A. J., Cowie, L. L., Steffen, A. T., Hornschemeier, A. E., Brandt, W. N., & Garmire, G. P. 2001, ApJ, 560, L23
Barger, A., et al. 2003, AJ, 126, 623
Bauer, F. E., et al. 2004, AJ, 128, 2048
Bavouzet, N. 2009, Thèse de Doctorat, Université Paris Sud 11
Blain, A. W., Smail, I., Ivison, R. J., Kneib, J.-P., & Frayer, D. T. 2002, Phys. Rep., 369, 111
Borys, C., Smail, I., Chapman, S. C., Blain, A. W., Alexander, D. M., & Ivison, R. J. 2005, ApJ, 635, 853
Bundy, K., et al. 2008, ApJ, 681, 931
Chabrier, G. 2003, PASP, 115, 763
Colbert, E. J. M., Weaver, K. A., Krolik, J. H., Mulchaey, J. S., & Mushotzky, R. F. 2002, ApJ, 581, 182
Cooper, M. C., et al. 2008, MNRAS, 383, 1058
Coppin, K., Halpern, M., Scott, D., Borys, C., & Chapman, S. 2005, MNRAS, 357, 1022
Coppin, K., et al. 2006, MNRAS, 372, 1621
Coppin, K., et al. 2009, MNRAS, 395, 1905
Cusumano, G. 2009, in AIP Conf. Proc. 1126, Simbol-X: Focusing on the Hard X-Ray Universe, ed. J. Rodriguez & P. Ferrando (Melville, NY: AIP), 104
Daddi, E., et al. 2007, ApJ, 670, 156
Elbaz, D., et al. 2007, A&A, 468, 33
Elvis, M., et al. 1994, ApJS, 95, 1
Evans, A.S, Frayer, D. T., Surace, J. A., & Sanders, D. B. 2001, AJ, 121, 3286
Fabian, A. C. 1999, MNRAS, 308, L39
Fabian, A. C., et al. 2000, MNRAS, 315, L8
Förster Schreiber, N. M., et al. 2006, ApJ, 645, 1062
Genzel, R., et al. 2008, ApJ, 687, 59
Giacconi, R., et al. 2002, ApJS, 139, 369
Granato, G. L., de Zotti, G., Silva, L., Bressan, A., & Danese, L. 2004, ApJ, 600, 580
Greve, T., et al. 2009, ApJ, submitted (arXiv:0904.0028)
Grogin, N. A., et al. 2005, ApJ, 627, L97
Güsten, R., Nyman, L. Å., Schilke, P., Menten, K., Cesarsky, C., & Booth, R. 2006, A&A, 454, L13
Häring, N., & Rix, H. W. 2004, ApJ, 604, L89
Hasinger, G. 2008, A&A, 490, 905
Holland, W. S., et al. 1999, MNRAS, 303, 659
Hopkins, P. F., & Hernquist, L. 2009, ApJ, 694, 599
Hopkins, P. F., Hernquist, L., Cox, T. J., Di Matteo, T., Robertson, B., & Springel, V. 2006, ApJS, 163, 1
Hornschemeier, A. E., et al. 2000, ApJ, 541, 49
Houck, J., et al. 2005, ApJ, 622, L105
Ivison, R. J., et al. 2007, MNRAS, 380, 199
Kauffmann, G., et al. 2003, MNRAS, 346, 1055
Kennicutt, R. C. 1998, ARA&A, 36, 189
Koekemoer, A., et al. 2004, ApJ, 600, L123
Lehmer, B. D., et al. 2005, ApJS, 161, 21
Lehmer, B. D., et al. 2008, ApJ, 681, 1163
Le Fevre, O., et al. 2004, A&A, 428, 1043
Le Floc'h, E., Mirabel, I. F., Laurent, O., Charmandaris, V., Gallais, P., Sauvage, M., Vigroux, L., & Cesarsky, C. 2001, A&A, 367, 487
Luo, B., et al. 2008, ApJS, 179, 19
Lutz, D., et al. 2005, ApJ, 625, L83
Lutz, D., et al. 2008, ApJ, 684, 853
Maiolino, R., et al. 2007, A&A, 468, 979
Mainieri, V., et al. 2005a, MNRAS, 356, 1571
Mainieri, V., et al. 2005b, A&A, 437, 805
Marconi, A., & Hunt, L. K 2003, ApJ, 689, L21
Miller, N., Fomalont, E. B., Kellermann, K. I., Mainieri, V., Norman, C., Padovani, P., Rosati, P., & Tozzi, P. 2008, ApJS, 179, 114
Mullaney, J. R., Alexander, D. M., Huynh, M., Goulding, A. D., & Frayer, D. 2010, MNRAS, 401, 995
Nandra, K., et al. 2007, ApJ, 660, L11
Negrello, M., González-Nuevo, J., Magliochetti, M., Moscardini, L., de Zotti, G., Toffolatti, L., & Danese, L. 2005, MNRAS, 358, 869
Nenkova, M., Sirocky, M. M., Nikutta, R., Ivezic, Z., & Elitzur, M. 2008, ApJ, 685, 160
Netzer, H. 2009, MNRAS, 399, 1907
Netzer, H., & Trakhtenbrot, B. 2007, ApJ, 564, 754
Netzer, H., et al. 2007, ApJ, 666, 806
Noeske, K. G., et al. 2007, ApJ, 660, L43

Norman, C., et al. 2002, ApJ, 571, 218

Omont, A., Beelen, A., Bertoldi, F., Cox, P., Carilli, C. L., Priddey, R. S., McMahon, R. G., & Isaak, K. G. 2003, A&A, 398, 857

Page, M. J., Mittaz, J. P. D., & Carrera, F. J. 2001, MNRAS, 325, 575

Page, M. J., Stevens, J. A., Ivison, R. J., & Carrera, F. J. 2004, ApJ, 611, L85

Page, M. J., Stevens, J. A., Mittaz, J. P. D., & Carrera, F. J. 2001, Science, 294, 2516

Papadopoulos, P. P., & Seaquist, E. R. 1999, ApJ, 514, L95

Pier, E. A., & Krolik, J. H. 1992, ApJ, 401, 99

Pier, E. A., & Krolik, J. H. 1993, ApJ, 418, 673

Pierce, C. M., et al. 2007, ApJ, 660, L19

Priddey, R. S., Isaak, K. G., McMahon, R. G., & Omont, A. 2003, MNRAS, 339, 1183

Rigopoulou, D., et al. 2009, MNRAS, 400, 1199

Roche, N. D., Dunlop, J., Caputi, K. L., McLure, R., Willott, C. J., & Crampton, D. 2006, MNRAS, 370, 74

Rovilos, E., Georgakakis, A., Georgantopoulos, I., Afonso, J., Koekemoer, A. M., Mobasher, B., & Goudis, C. 2001, A&A, 466, 119

Rowan-Robinson, M. 1995, MNRAS, 272, 737

Sanders, D. B., Soifer, B. T., Elias, J. H., Madore, B. F., Matthews, K., Neugebauer, G., & Scoville, N. Z. 1988, ApJ, 325, 74

Schweitzer, M., et al. 2006, ApJ, 649, 79

Severgnini, P., et al. 2000, A&A, 360, 457

Shapiro, K. L., et al. 2008, ApJ, 682, 231

Silverman, J. D., et al. 2008, ApJ, 675, 1025

Silverman, J. D., et al. 2009, ApJ, 696, 396

Siringo, G., et al. 2009, A&A, 497, 945

Solomon, P. M., & VandenBout, P. A. 2005, ARA&A, 43, 677

Steffen, A., et al. 2006, AJ, 131, 2826

Stevens, J. A., Page, M. J., Ivison, R. J., Carrera, F. J., Mittaz, J. P. D., Smail, I., & McHardy, I. M. 2005, MNRAS, 360, 610

Sturm, E., Hasinger, G., Lehmann, I., Mainieri, V., Genzel, R., Lehnert, M. D., Lutz, D., & Tacconi, L. J. 2006, ApJ, 642, 81

Szokoly, G., et al. 2004, ApJS, 155, 271

Tozzi, P., et al. 2006, A&A, 451, 457

Treister, E., et al. 2009, ApJ, 691, 1713

Trichas, M., Georgakakis, A., Rowan-Robinson, M., Nandra, K., Clements, D., & Vaccari, M. 2009, MNRAS, 399, 663

Tueller, J., Mushotzky, R. F., Barthelmy, S., Cannizzo, J. K., Gehrels, N., Markwardt, C. N., Skinner, G. K., & Winter, L. M. 2008, ApJ, 681, 113

Waskett, T. J., et al. 2003, MNRAS, 341, 1217

Weiß, A., et al. 2009, ApJ, 707, 1201

Wolf, C., Hildebrandt, H., Taylor, E. N., & Meisenheimer, K. 2008, A&A, 491, 933

Wolf, C., et al. 2004, A&A, 421, 913

Zakamska, N.L, Gómez, L., Strauss, M. A., & Krolik, J. H. 2008, AJ, 136, 1607